Super- and sub-rotating equatorial jets: Newtonian cooling versus Rayleigh friction

Emma S. Warneford† and Paul J. Dellar

OCIAM, Mathematical Institute, University of Oxford, Radcliffe Observatory Quarter, Woodstock Road, Oxford, OX2 6GG, UK

(Received 24 January 2014)

arXiv:1401.6406v1 [physics.flu-dyn] 24 Jan 2014

Numerical simulations of the standard shallow water equations on a rotating sphere produce a mixture of robust vortices and alternating zonal jets, like those seen in the atmospheres of the gas giant planets. However, simulations that include Rayleigh friction invariably produce a sub-rotating (retrograde) equatorial jet for Jovian parameter regimes, whilst observations of Jupiter show that a super-rotating (prograde) equatorial jet has persisted over several decades. Super-rotating equatorial jets have recently been obtained in simulations that model radiative cooling to space by a Newtonian relaxation of perturbations in the shallow water height field, and in simulations of the thermal shallow water equations that include a similar cooling term in their separate temperature equation. We provide an explanation for the directions of the equatorial jets in these different models by calculating the effects of the two forms of dissipation, Newtonian cooling and Rayleigh friction, upon the momentum transport induced by equatorially trapped Rossby waves. In the absence of dissipation, these waves produce zero net transport of zonal momentum in the meridional direction. However, dissipation alters the phase relation between the zonal and meridional velocity fluctuations responsible for this cancellation. Dissipation by Newtonian leads to a positive zonal mean zonal acceleration, consistent with the formation of super-rotating equatorial jets, while dissipation by Rayleigh friction leads to a negative zonal mean zonal acceleration, consistent with the formation of sub-rotating equatorial jets.

1. Introduction

Observations of Jupiter's atmosphere reveal a highly turbulent cloud deck, in which long-lived coherent vortices such as the Great Red Spot are transported around the planet by an alternating pattern of zonal jets. Figure 1 shows Jupiter's mean zonal wind profile, as derived from feature tracking in images taken by the Voyager 2 (Limaye 1986) and Cassini (Porco *et al.* 2003) missions. The similarity of these two profiles, taken from missions over 20 years apart, demonstrates the remarkable stability of Jupiter's zonal winds, and the presence of a broad, super-rotating equatorial jet. Vasavada & Showman (2005) recently reviewed the current state of observational data, theory, experiments, and simulations related to Jupiter's atmosphere. Almost all data comes from remote observations, with the exception of a single descent by the Galileo probe which measured unidirectional horizontal winds that were roughly uniform from a depth of 4 bars down to 22 bars, and some stable stratification over this range of depths (Atkinson *et al.* 1998).

Following the pioneering non-divergent barotropic model of Williams (1978), shallow water theory has been widely applied to the Jovian atmosphere (Cho & Polvani 1996*a*,*b*; Dowling & Ingersoll 1989; Iacono *et al.* 1999*a*,*b*; Ingersoll 1990; Marcus 1988; Scott & Polvani 2007, 2008; Showman 2007; Williams & Yamagata 1984). The cloud deck is treated as a homogeneous layer separated from a much deeper and relatively quiescent lower layer by a sharp density contrast, which may be linked to the latent heat released by water vapour condensing at this depth. The equivalent barotropic approximation (Dowling & Ingersoll 1989; Gill 1982) gives a closed set of shallow water equations for the cloud deck that contains the reduced gravity $g' = g\Delta\rho/\rho_0$. Here g is the actual gravitational acceleration, $\Delta\rho$ is the density contrast between the two layers, and ρ_0 is a reference density. Confidence in the validity of this model has been reinforced by observations of what appear to be internal gravity waves radiating from the impact points of Shoemaker–Levy comet debris (Dowling 1995; Ingersoll *et al.* 2007), although this interpretation is not without its critics (Walterscheid *et al.* 2000).

Numerical simulations of the standard shallow water equations (defined below by (1.1) with infinite $\tau_{\rm rad}$) on rotating spheres with Jovian parameter values reproduce a mixture of robust vortices and alternating zonal jets. The latter arise naturally through the coupling to Rossby waves that arrests the turbulent inverse cascade at the scale identified by Rhines (1975). However, the jet at the equator is invariably sub-rotating (retrograde) in both freely decaying and forced-dissipative simulations in the Jovian regime (e.g. Cho & Polvani 1996*a*,*b*; Iacono *et al.* 1999*a*,*b*; Scott & Polvani 2007; Showman 2007). This is in sharp contrast to the prominent super-rotating equatorial jet that has persisted for decades on Jupiter (see figure 1). According to Hide's (1969) theorem, this jet must be maintained by an upgradient eddy flux of angular momentum.

† Email address for correspondence: emma.warneford@maths.ox.ac.uk

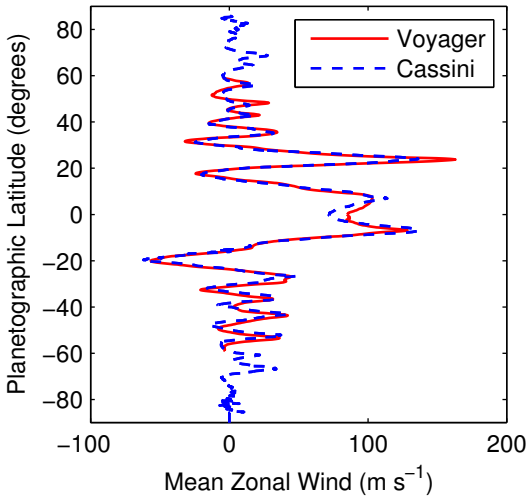

FIGURE 1. Mean zonal wind profiles for Jupiter. The red solid line shows Voyager 2 data from Limaye (1986) and the blue dashed line shows Cassini data from Porco *et al.* (2003).

Forced-dissipative shallow water simulations typically include a Rayleigh friction term to absorb the slow leakage of energy past the Rhines scale to the largest scales in the system. Unless dissipated, this leakage eventually causes the pattern of alternating zonal jets to break up into large coherent vortices (Vasavada & Showman 2005). Scott & Polvani (2007, 2008) added an additional Newtonian cooling term to the continuity equation in their shallow water model,

$$h_t + \boldsymbol{\nabla}\cdot(h\boldsymbol{u}) = -(h-h_0)/\tau_{\rm rad}, \tag{1.1a}$$

$$\boldsymbol{u}_t + (\boldsymbol{u}\cdot\boldsymbol{\nabla})\,\boldsymbol{u} + f\hat{\boldsymbol{z}}\times\boldsymbol{u} = -g'\boldsymbol{\nabla}h + \boldsymbol{F} - \boldsymbol{u}/\tau_{\rm fric}, \tag{1.1b}$$

following earlier models of the terrestrial stratosphere (Juckes 1989; Polvani *et al.* 1995). Here h is the height of the active layer, $\boldsymbol{u}$ is the depth-averaged horizontal velocity, $f = 2\Omega\sin\phi$ is the Coriolis parameter at latitude ϕ on a planet rotating with angular velocity Ω, $\boldsymbol{\nabla}$ is the horizontal gradient operator, $\hat{\boldsymbol{z}}$ is a unit vector in the local vertical direction, $\boldsymbol{F}$ is an isotropic random forcing, and $\tau_{\rm fric}$ is the time scale of Rayleigh friction. The right-hand side of (1.1a) models the effects of radiation to space with a Newtonian cooling of h towards its constant mean value h_0 on the time scale $\tau_{\rm rad}$. Scott & Polvani's (2007; 2008) simulations of this system with only Newtonian cooling as dissipation (infinite $\tau_{\rm fric}$) produced a sharply localised super-rotating equatorial jet, as do our subsequent simulations reported in §2 and Warneford & Dellar (2014) for plausible Jovian values of $\tau_{\rm rad}$ and the other parameters.

Warneford & Dellar (2014) presented the thermal shallow water equations as an alternative model for Jupiter. These equations were introduced by Lavoie (1972) to describe atmospheric mixed layers over frozen lakes, and later adopted for tropical and coastal oceans, and the upper ocean mixed layer (McCreary *et al.* 1991; McCreary & Kundu 1988; McCreary & Yu 1992; Røed & Shi 1999; Schopf & Cane 1983). Their theoretical properties were developed by Ripa (1993, 1995, 1996*a*,*b*). While standard shallow water theory applies to one or more layers of homogeneous fluid, thermal shallow water theory permits horizontal variations of the thermodynamic properties of the fluid within each layer. The density contrast $\Delta\rho$ is then spatially varying. We introduce the symbol $\Theta = g\Delta\rho/\rho_0$ for the reduced gravity to emphasise that it is now a function of space and time. The thermal shallow water equations are given by

$$h_t + \boldsymbol{\nabla}\cdot(h\boldsymbol{u}) = 0, \tag{1.2a}$$

$$\Theta_t + (\boldsymbol{u}\cdot\boldsymbol{\nabla})\,\Theta = -(\Theta h/h_0 - \Theta_0)/\tau_{\rm rad}, \tag{1.2b}$$

$$\boldsymbol{u}_t + (\boldsymbol{u}\cdot\boldsymbol{\nabla})\,\boldsymbol{u} + f\hat{\boldsymbol{z}}\times\boldsymbol{u} = -\boldsymbol{\nabla}(\Theta h) + \tfrac{1}{2}h\boldsymbol{\nabla}\Theta + \boldsymbol{F} - \boldsymbol{u}/\tau_{\rm fric}. \tag{1.2c}$$

The right-hand side of (1.2b) is a Newtonian cooling term that represents radiative relaxation towards a constant temperature $\Theta_0 h_0/h$ with time scale $\tau_{\rm rad}$. The h-dependence models the more effective radiation from columns that extend higher. These thermal shallow water equations conserve both mass and momentum when $\tau_{\rm fric}$ is infinite and $\boldsymbol{F} = \boldsymbol{0}$, unlike the Scott and Polvani model (1.1). Simulations of the thermal shallow water equations for Jovian parameter values (reported in §2 and Warneford & Dellar 2014) reproduce a super-rotating equatorial jet, and more substantial mid-latitude jets than simulations of the Scott & Polvani (2007, 2008) model. Henceforth, for brevity we refer to the Newtonian cooling terms as cooling and the Rayleigh friction term as friction.

Equatorially trapped waves play an important role in near-equatorial dynamics (e.g. Gill 1982; Khouider *et al.* 2013; Majda & Klein 2003; McCreary 1985). In this paper we investigate the role of these waves in establishing the

a	$2\pi/\Omega$	$\sqrt{g'h_0}$	g	$\tau_{\rm rad}$	$\tau_{\rm fric}$
7.1×10^7m	9.9 hours	$678\,\mathrm{m\,s^{-1}}$	$26\,\mathrm{m\,s^{-2}}$	429 hours	9900 hours

TABLE 1. Parameter values for Jupiter (from Beebe 1994; Ingersoll 1990; Warneford & Dellar 2014).

direction of the equatorial jet. They are conveniently studied using the equatorial beta-plane approximation, expressed in Cartesian geometry with a latitude-dependent Coriolis parameter, that is valid within about 30° of the equator. Expanding $f = 2\Omega\sin\phi$ around the equator gives $f(y) \approx \beta y$, where $\beta = 2\Omega/a$, $y = a\phi$, and a is the radius of the planet. The shallow water equations on the equatorial beta-plane (with no dissipation or forcing) support a spectrum of equatorially trapped westward-propagating Rossby waves, originally discovered by Matsuno (1966), and described in §3.

Our focus on Rossby waves is motivated by quasi-geostrophic (QG) theory, which offers a simplified description of slow vortical motion that filters out inertia-gravity waves. Although usually employed for mid-latitude beta-planes, Kuo (1959) and Charney & Stern (1962) presented a global QG theory for fully stratified atmospheres on spheres. Verkley (2009) and Schubert *et al.* (2009) revived this theory for the standard shallow water equations on a sphere in the form

$$\partial_t q + [\psi, q] = 0, \quad (f/\mathit{Ro}) + \nabla^2\psi - (f^2/\mathit{Bu})\psi = q, \tag{1.3}$$

where $[\psi, q] = \hat{\boldsymbol{z}}\cdot(\boldsymbol{\nabla}\psi\times\boldsymbol{\nabla}q)$, and *Bu* and *Ro* are the Burger and Rossby numbers respectively. The sole evolving variable is the potential vorticity q, which is advected by the velocity field derived from a streamfunction ψ. The elliptic equation relating ψ to q involves the spatially varying Coriolis parameter f. It reduces to the standard beta-plane QG form on approximating f by $f_0 + \beta y$ in the first term, and by f_0 in the second term. Warneford (2014) presents a thermal form of this global QG theory, building on the local thermal QG equations in Ripa (1996*b*) and Warneford & Dellar (2013). Numerical simulations of the global thermal QG equations reported in Warneford (2014) produce a super-rotating equatorial jet when the dimensionless cooling time is sufficiently short, as do simulations of the global QG form of Scott & Polvani's (2007; 2008) height-damped shallow water model. Simulations of the latter model without height damping produce a sub-rotating equatorial jet. The global QG forms of the three different shallow water models produce equatorial jets in the same directions as their parent models. The mechanism responsible for setting the direction of equatorial jets must therefore lie within QG theory, which justifies our subsequent neglect of the inertia-gravity, Kelvin and Yanai waves.

In calculating the transport of zonal momentum by Rossby waves, our approach represents a shallow water version of Andrews & McIntyre's (1976) study of the competing effects of friction and cooling on equatorial Rossby waves in a three-dimensional stratified atmosphere. A key difference is that the mean zonal accelerations at the equator calculated by Andrews & McIntyre (1976) were always westward ($\langle u\rangle_t \leqslant 0$ in the notation of §4) and so could not explain the formation of super-rotating equatorial jets. However, Andrews & McIntyre (1976) studied the limit of large vertical wavenumber for waves in a stratified fluid, while shallow water theory describes the opposite limit of zero vertical wavenumber. Imamura *et al.* (2004) performed a similar analysis for a modified equatorial Kelvin wave solution in the presence of a zonal mean meridional circulation. This solution possessed a non-zero meridional wave component which induced a meridional flux of zonal momentum. Showman & Polvani (2011) recently looked at a variant of the Matsuno–Gill problem for the response due to a steady longitudinally-varying forcing as a model for solar forcing on a tidally locked exoplanet. They found that the interaction between the resulting standing Rossby and Kelvin waves generated a super-rotating equatorial jet, but this model relies on a tidally-locked solar forcing, and so does not apply to Jupiter with its 9.9 hour rotation period. Arnold *et al.* (2012) found super-rotation in an idealized multilevel GCM forced with a zonally varying equatorial heating, and identified a Rossby–Kelvin wave resonance as being responsible for eddy momentum flux convergence at the equator. However, their theory requires an equatorial source of Rossby waves, which is not visible in our simulations (see figure 6 in §2).

2. Numerical experiments

In this section we show numerical solutions of the Scott & Polvani (2007, 2008) model and the thermal shallow water model. First we consider a standard shallow water simulation that contains just friction (i.e. (1.1) with infinite $\tau_{\rm rad}$), secondly we consider a height-damped simulation that contains both cooling and friction (1.1), and finally we consider a thermal shallow water simulation that contains both cooling and friction (1.2). Typical values of the relevant parameters for Jupiter are given in table 1, where a is the planetary radius, Ω is the angular velocity, $\sqrt{g'h_0}$ is the gravity wave speed and g is the gravity. $\tau_{\rm rad}$ is the time scale we use for cooling where relevant, and arises by considering a 200km deep weather layer with an upper temperature of 120K. It corresponds to a time scale of 43 Jovian days. All simulations contain friction with a time scale $\tau_{\rm fric}$ defined in table 1, which corresponds to 1000 Jovian days. Comparing the radius

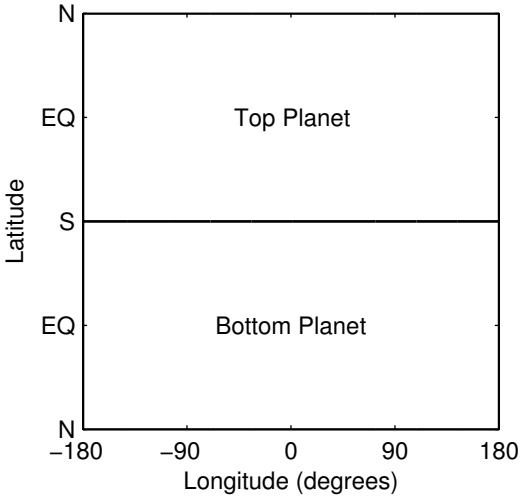

FIGURE 2. Schematic of the doubly-periodic Cartesian domain used for the numerical simulations. Each half of the domain represents a full planet, so for clarity we show simulation results for just the top planet.

of the planet with the deformation radius for Jupiter $L_{\mathrm{D}} = \sqrt{g'h_0}/(2\Omega)$, we find that there are 232 deformation radii around the circumference, based on the internal wave speed deduced from impacts of Shoemaker–Levy comet debris (Dowling 1995; Ingersoll *et al.* 2007). We set $\Theta_0 = g'$ for the thermal shallow water simulation.

We solve the equation sets in the doubly-periodic Cartesian domain sketched in figure 2, which we refer to as the square planet domain. The horizontal axis denotes longitude, while the vertical axis denotes latitude. Starting from the north pole at the top of the domain and moving down, we reach the equator a quarter of the way down, and the south pole half way down. We then continue to reach the equator again, before returning to the north pole at the bottom of the domain. We imagine following a meridian (constant longitude line) from the north pole to the equator to the south pole, and then following a second meridian with longitude offset by 180° back across the equator to the north pole. The Coriolis force is still fully varying in latitude and is defined in the simulations by $f(y) = 2\Omega\cos(2\pi y/y_{\max})$, where $y_{\max}$ is the length of the side of the square planet domain, i.e. the circumference of Jupiter (see table 1). Thus the Coriolis force and all its derivatives are doubly periodic. Simulations of geostrophic turbulence in the Jovian regime require many rotation periods to reach statistically steady states. This doubly-periodic Cartesian geometry allows us to exploit the superior memory bandwidth and floating point performance of graphical processing units (GPUs) using a spectral spatial representation based on fast Fourier transforms, while the performance of existing spherical harmonic transforms for GPUs remains comparable with that of conventional microprocessors (Hupca *et al.* 2012). Each half of the square planet domain corresponds to a complete planet, so we plot our simulation results only for the top planet in figure 2.

Following Scott & Polvani (2007, 2008) we drive the flow by applying a divergence-free isotropic random forcing $\boldsymbol{F}$ that is localised to a narrow annulus of wavenumbers $|\mathbf{k}| \in [k_c - 2, k_c + 2]$ in Fourier space. We set $k_c = 42$ for a direct comparison to Scott & Polvani (2008), counting wavenumbers from the longest sinusoidal mode in the domain being wavenumber 1. We force each mode inside this annulus with amplitude ϵ_f using random phases that are δ-correlated (white) in time. Originally due to Lilly (1969), this type of forcing is widely used in numerical studies of zonal jet formation (Smith 2004; Smith *et al.* 2002; Srinivasan & Young 2012). It may be interpreted as a model for energy injected by three-dimensional convection at horizontal lengthscales comparable to the deformation radius. Our simulations dynamically adjust the amplitude of the forcing ϵ_f to give a prescribed value for the total kinetic energy in the eventual statistical steady state.

The shallow water equations are discretized using a standard pseudospectral technique on a grid of 1024×1024 Fourier collocation points. The resulting large system of ordinary differential equations is integrated using the standard fourth-order Runge–Kutta scheme, with a time step determined dynamically from the Courant–Friedrichs–Lewy stability condition. We use the Hou & Li (2007) spectral filter to control the build-up of enstrophy at the highest wavenumbers. We take $h = h_0$ and $u = v = 0$ as initial conditions for all runs, and $\Theta = \Theta_0$ for the thermal shallow water simulation. Full details of the numerical model, parameters, and further simulation outputs may be found in Warneford & Dellar (2014).

Figure 3 shows the instantaneous absolute vorticity $\omega_{\mathrm{a}} = v_x - u_y + f(y)$ after 2×10^4 Jovian rotation periods for the top planet in figure 2 for the three simulation runs. Figure 4 shows the corresponding instantaneous zonal velocity plots, and figure 5 shows the instantaneous zonally averaged zonal velocity, $\langle u\rangle = x_{\max}^{-1}\int u(x,y,t)\,\mathrm{d}x$, where $x_{\max}$ is

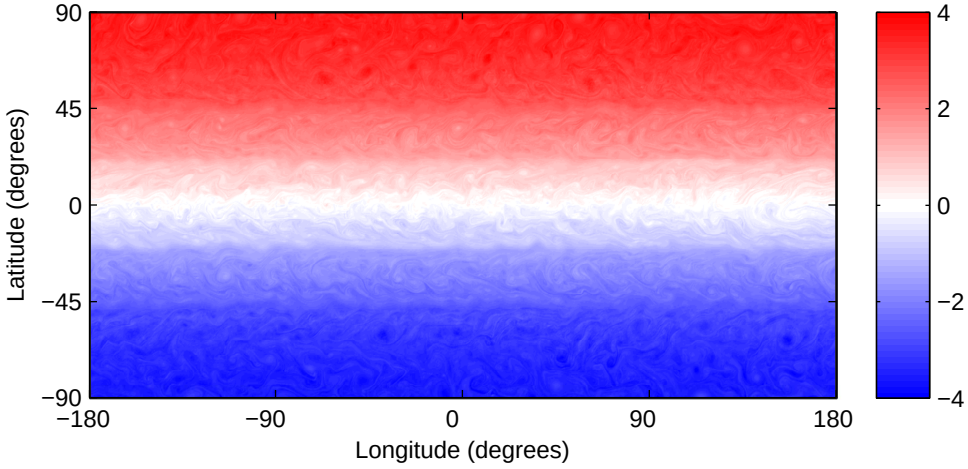

(a)

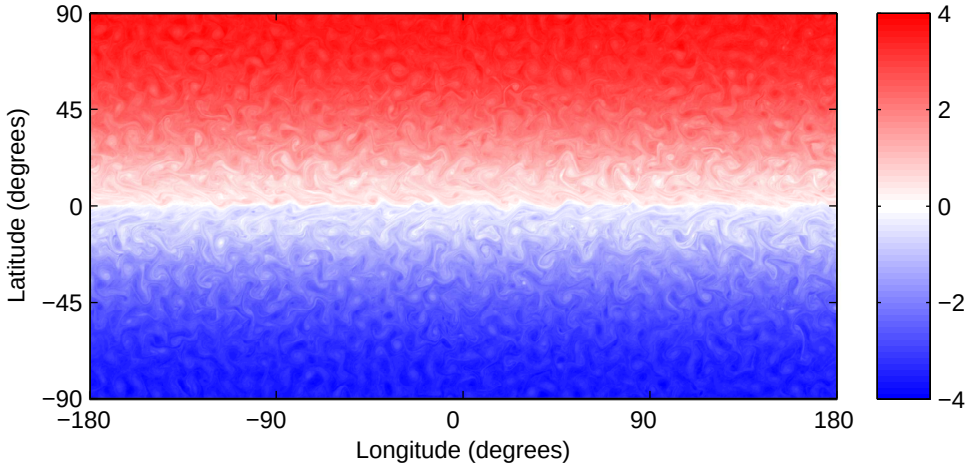

(b)

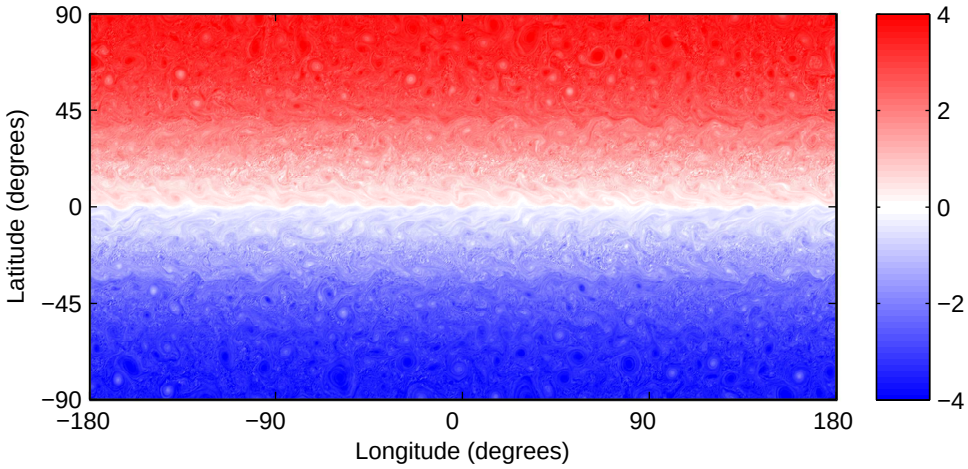

(c)

FIGURE 3. Absolute vorticity $\omega_{\mathrm{a}} = v_x - u_y + f(y)$ in units of 10^{-4} s^{-1} for (a) a standard shallow water simulation with dissipation by friction alone, (b) a height-damped shallow water simulation with dissipation by cooling and friction, and (c) a thermal shallow water simulation with dissipation by cooling and friction.

the side length of the square planet domain shown in figure 2. All three simulation runs exhibit a mixture of vortices, turbulence and multiple zonal jets, with amplitudes that decrease at higher latitudes. Our height-damped and thermal shallow water simulations, which both included cooling and friction, produced a strong super-rotating equatorial jet in line with Jovian observations. However, our simulation of the standard shallow water model, with dissipation only by friction, produced a sub-rotating equatorial jet. The height-damped shallow water simulation only produced very weak jets away from the equator, whereas the standard and thermal shallow water simulations produced stronger mid-latitude jets in better agreement with Jovian observations.

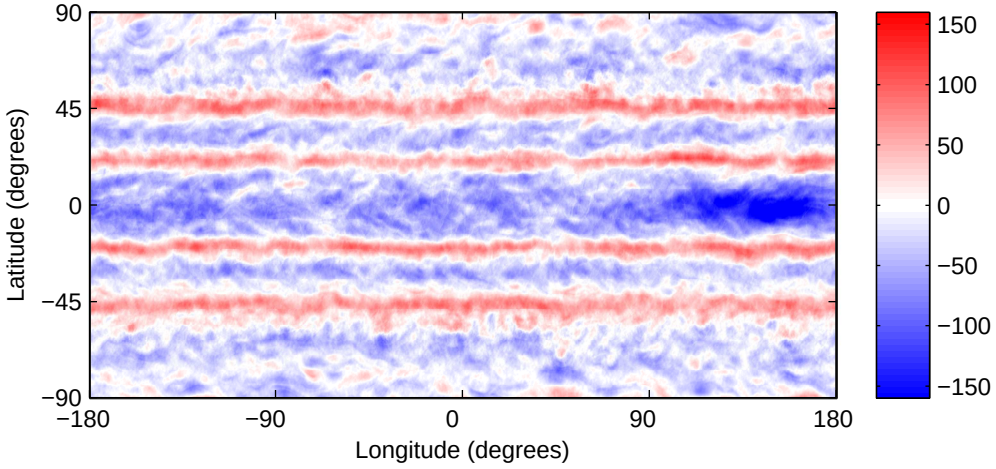

(a)

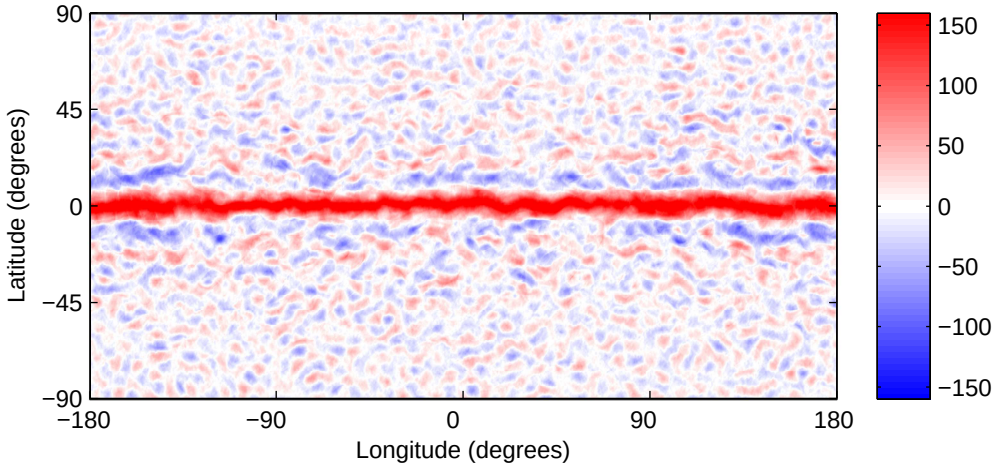

(b)

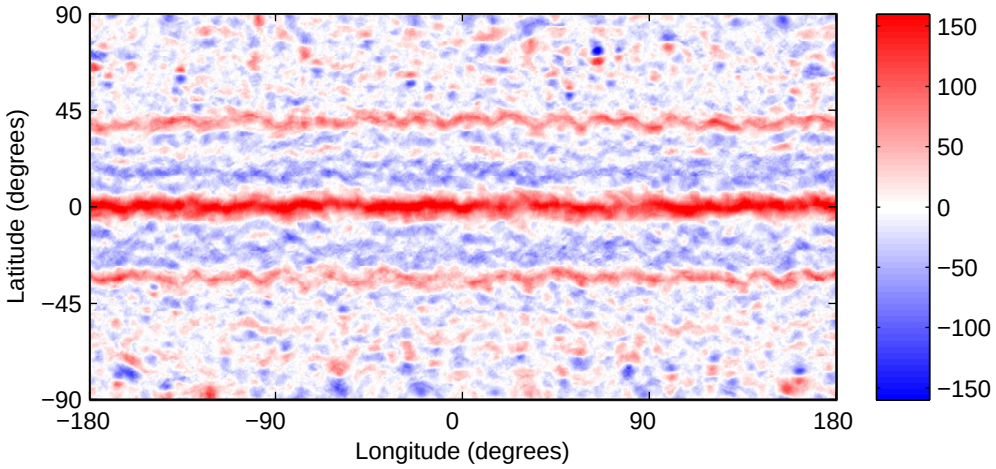

(c)

FIGURE 4. Zonal velocity u in units of m s^{-1} for (a) a standard shallow water simulation with dissipation by friction alone, (b) a height-damped shallow water simulation with dissipation by cooling and friction, and (c) a thermal shallow water simulation with dissipation by cooling and friction.

Sardeshmukh & Hoskins (1988) introduced a diagnostic for sources of Rossby wave activity using a Helmholtz decomposition of the velocity $\boldsymbol{u} = \boldsymbol{u}_\chi + \boldsymbol{u}_\psi$ into divergent ($\boldsymbol{u}_\chi$) and rotational ($\boldsymbol{u}_\psi$) parts. The absolute vorticity $\omega_\mathrm{a} = f(y) + v_x - u_y$ in the height-damped shallow water equations evolves according to

$$\partial_t \omega_\mathrm{a} + (\boldsymbol{u}_\psi \cdot \boldsymbol{\nabla})\, \omega_\mathrm{a} = R + \hat{\boldsymbol{z}} \cdot \boldsymbol{\nabla} \times \boldsymbol{F} - (\omega_\mathrm{a} - f(y))\,/\tau_\mathrm{fric}, \tag{2.1}$$

where $R = -\boldsymbol{\nabla} \cdot (\omega_\mathrm{a} \boldsymbol{u}_\chi)$ is identified as the source of Rossby wave activity. The corresponding equation for our thermal shallow water model adds a baroclinic torque $(1/2)\hat{\boldsymbol{z}} \cdot (\boldsymbol{\nabla} h \times \boldsymbol{\nabla} \Theta)$ to the right-hand side. We follow Schneider & Liu

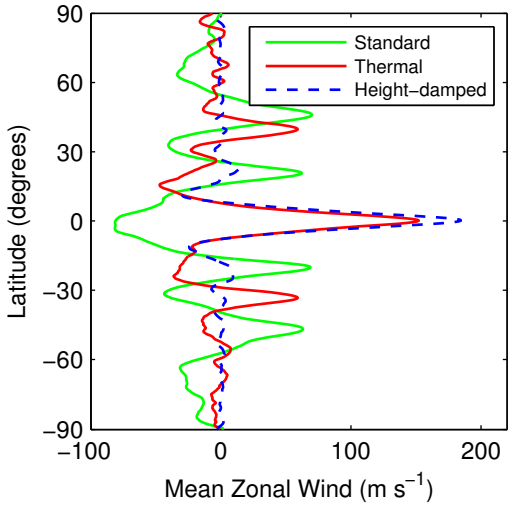

FIGURE 5. Mean zonal velocity $\langle u \rangle$ against latitude for a standard shallow water simulation with dissipation by friction alone, a height-damped shallow water simulation with dissipation by cooling and friction, and a thermal shallow water simulation with dissipation by cooling and friction.

(2009) in using the nonzonal part $R' = R - \langle R \rangle$ to diagnose sources of Rossby wave activity in our different models. Figure 6 shows the instantaneous R' field at 2×10^4 Jovian days for our three different simulations, and figure 7 shows the corresponding root-mean-square zonal averages $\langle R'^2 \rangle^{1/2}$. Rossby waves are preferentially generated away from the equator in all three simulations, so we assume that any Rossby waves present in the near-equatorial region were excited by sources outside that region.

3. Rossby waves on an equatorial beta-plane

We now investigate the properties of equatorially trapped waves in the three different shallow water models in the presence of dissipation.

3.1. *Height-damped shallow water equations*

The linearised form of the unforced ($\boldsymbol{F} = \boldsymbol{0}$) height-damped shallow water equations (1.1) on an equatorial beta-plane may be written as (Gill 1982; Matsuno 1966)

$$h'_t + u'_x + v'_y = -\kappa h', \tag{3.1a}$$

$$u'_t - \tfrac{1}{2} y v' + h'_x = -\gamma u', \tag{3.1b}$$

$$v'_t + \tfrac{1}{2} y u' + h'_y = -\gamma v'. \tag{3.1c}$$

The dashes denote small perturbations about a rest state with uniform depth h_0. We have non-dimensionalised using the internal wave speed $c = \sqrt{g' h_0}$ as the velocity scale, the equatorial deformation radius $L_{\mathrm{eq}} = \sqrt{c/2\beta}$ as the horizontal length scale ($\beta = 2\Omega/a$), h_0 as the height scale, and the advective time scale $T = L_{\mathrm{eq}}/c$. Table 1 gives Jovian values of all these parameters. The dimensionless cooling and friction rates are $\kappa = T/\tau_{\mathrm{rad}}$ and $\gamma = T/\tau_{\mathrm{fric}}$, with values $\kappa = 0.00788$ and $\gamma = T/\tau_{\mathrm{fric}} = 0.000342$ in our Jovian simulations. In these variables, the latitude is $\phi = (L_{\mathrm{eq}}/a)y = \sqrt{Ro}\, y$ where $Ro = c/(4\Omega a)$ is the Rossby number based on the internal wave speed and the planetary diameter $2a$. The Jovian parameters in table 1 give $Ro \approx 0.014$, so $y = 5$ corresponds to a latitude of 33° in our subsequent plots.

Following Matsuno (1966) and Gill (1982) we seek waves that are harmonic in longitude and time, of the form $h'(x, y, t) = \mathrm{Re}\{\hat{h}(y) \exp(\mathrm{i}(kx - \omega t))\}$ etc. With no dissipation ($\kappa = \gamma = 0$) the three equations (3.1) may be combined into a single ordinary differential equation (ODE) for the meridional velocity $\hat{v}(y)$,

$$\frac{\mathrm{d}^2 \hat{v}}{\mathrm{d}y^2} = (Ay^2 - B)\hat{v}, \quad A = \frac{1}{4}, \quad B = \omega^2 - k^2 - \frac{k}{2\omega}, \tag{3.2}$$

the same equation that governs a quantum harmonic oscillator. The solutions that decay as $y \to \pm\infty$ may be written using the Hermite polynomials $H_n(\xi)$ as

$$\hat{v} = H_n(\xi) \exp(-\xi^2/2), \quad \xi = yA^{1/4}. \tag{3.3}$$

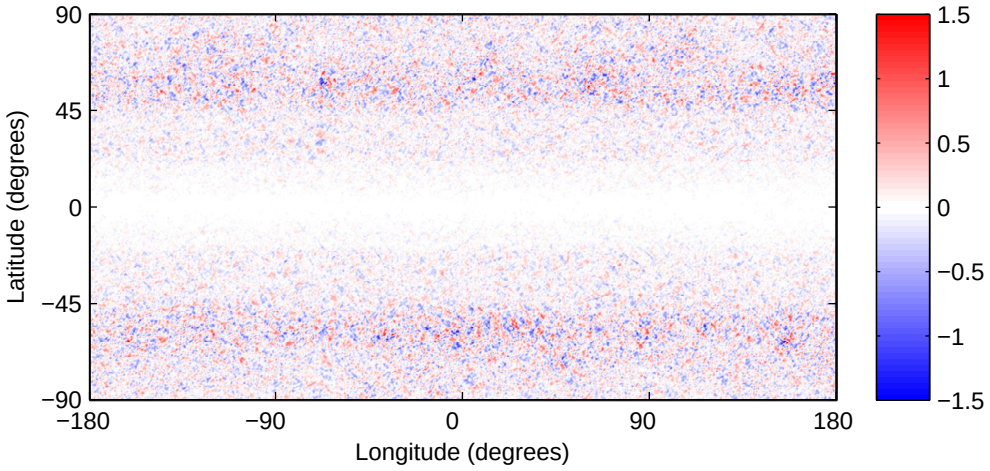

(a)

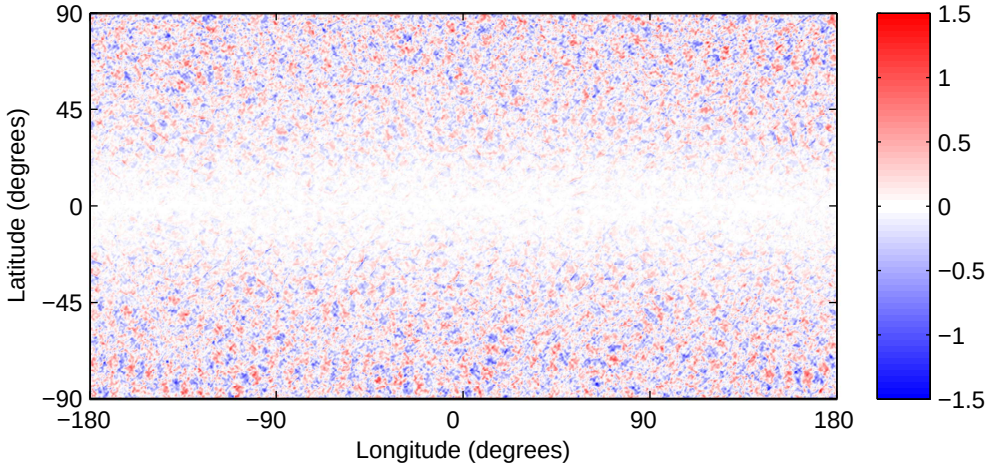

(b)

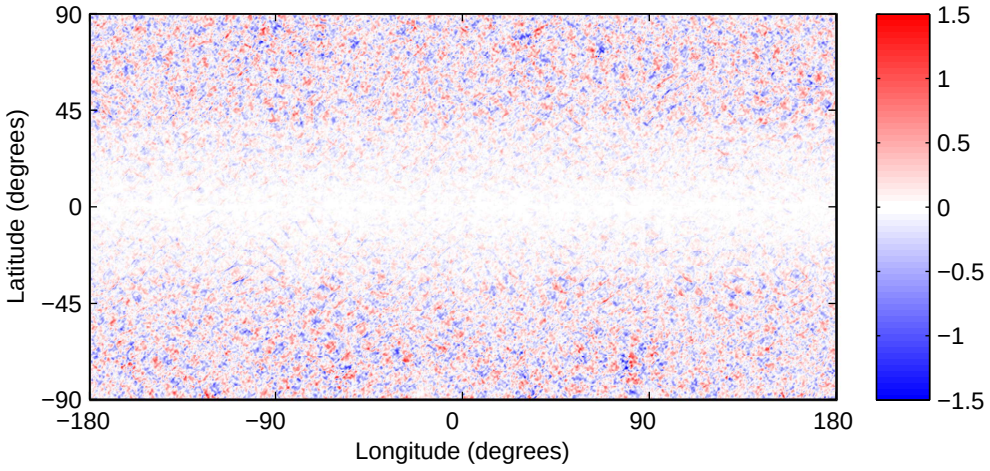

(c)

FIGURE 6. Rossby wave source R' in units of 10^{-8} s^{-2} for (a) a standard shallow water simulation with dissipation by friction alone, (b) a height-damped shallow water simulation with dissipation by cooling and friction, and (c) a thermal shallow water simulation with dissipation by cooling and friction.

The dispersion relation $A^{-1/2}B = 2n + 1$ for $n = -1, 0, 1, 2, \ldots$ gives a cubic equation for ω,

$$\omega^2 - k^2 - \frac{k}{2\omega} = n + \frac{1}{2}. \tag{3.4}$$

The Rossby wave branch of solutions is characterised by $n \geqslant 1$ and $0 < -\omega/k \ll 1$. The other two roots give inertia-gravity waves with $|\omega| \geqslant |k|$. The cases $n = 0$ and $n = -1$ give the Yanai and Kelvin waves respectively. Figure 8 shows these different branches of the dispersion relation, all of which represent trapped waves localised within

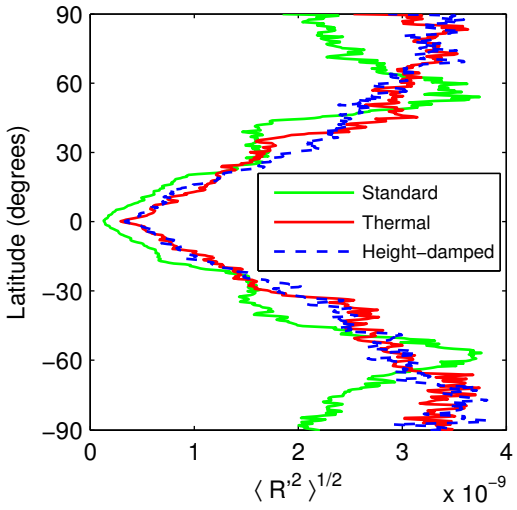

FIGURE 7. Zonal root-mean-square averages of the Rossby wave source fields shown in figure 6 for the standard, height-damped, and thermal shallow water simulations.

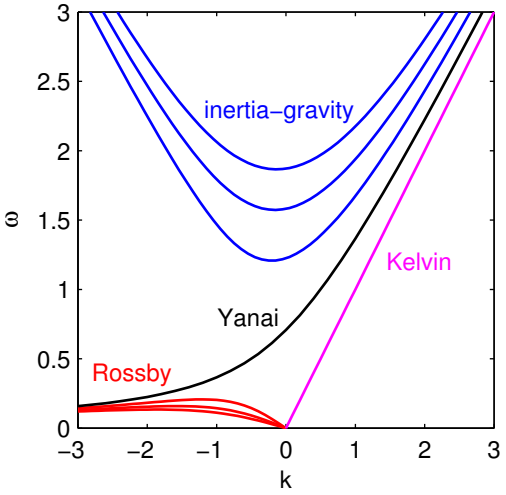

FIGURE 8. Dispersion relation for equatorially trapped waves in the standard shallow water equations with no dissipation (real ω) on the equatorial beta-plane.

a few deformation radii of the equator. The inertia-gravity, Yanai and Kelvin wave branches all enter the super-interial frequency regime $\omega \geqslant f$, and so do not exist in quasi-geostrophic theory.

Restoring the friction and cooling terms in (3.1) changes the A and B coefficients in the ODE to

$$A = \frac{1}{4}\left(\frac{\omega + \mathrm{i}\kappa}{\omega + \mathrm{i}\gamma}\right), \quad B = \omega^2 - k^2 - \frac{k}{2\,(\omega + \mathrm{i}\gamma)} + \mathrm{i}\omega\,(\kappa + \gamma) - \kappa\gamma, \tag{3.5}$$

so the dispersion relation becomes

$$\omega^2 - k^2 - \frac{k}{2(\omega + \mathrm{i}\gamma)} + \mathrm{i}\omega(\kappa + \gamma) - \kappa\gamma = \left(n + \frac{1}{2}\right)\left(\frac{\omega + \mathrm{i}\kappa}{\omega + \mathrm{i}\gamma}\right)^{1/2} \text{ for } n = 1, 2, \ldots. \tag{3.6}$$

Figure 9 shows the real and imaginary parts of the complex frequency ω for the first few equatorial Rossby waves ($n = 1, 2, 3$) for different values of γ and κ. The dispersion relation (3.4) shown in figure 8 is invariant under the transformation $(k, \omega) \to (-k, -\omega)$. We prefer to work with $k > 0$ and negative Rossby wave frequencies with $\mathrm{Re}(\omega) < 0$. The real part of ω is virtually unchanged for weak damping ($\kappa = 0.001$ or $\gamma = 0.001$), while $\mathrm{Im}(\omega)$ becomes negative as expected. The damping due to cooling ($\kappa = 0.001$ and $\gamma = 0$) is largest for small k, and tends to zero as $k \to \infty$. By contrast, the damping due to friction ($\gamma = 0.001$ and $\kappa = 0$) is monotonically increasing with k, being weakest for small k, and tending to $-\gamma$ as $k \to \infty$.

Figure 9(b) suggests a symmetry about the line $\mathrm{Im}(\omega) = -\epsilon/2$ between small cooling ($\kappa = \epsilon$ and $\gamma = 0$) and

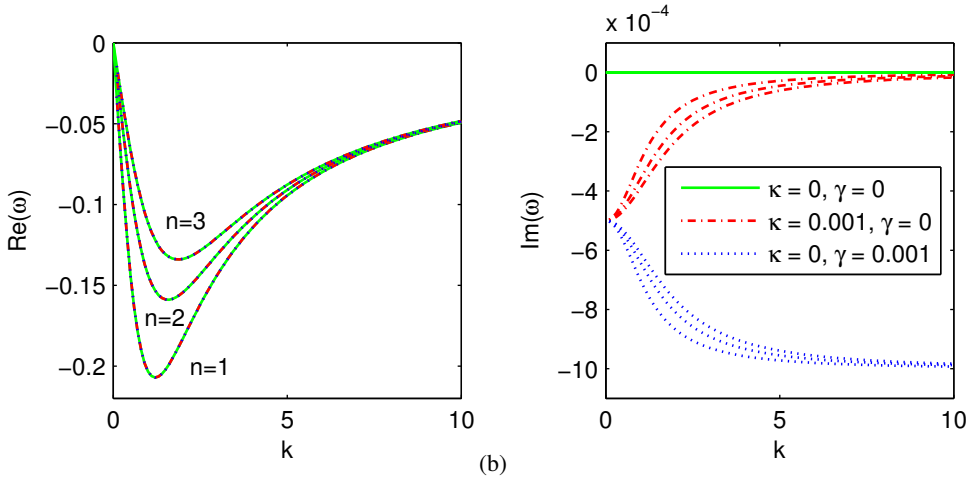

FIGURE 9. The (a) real and (b) imaginary parts of the dimensionless equatorial Rossby wave frequency ω for the height-damped shallow water model with no dissipation, dissipation by cooling alone, and dissipation by friction alone.

small friction ($\kappa = 0$ and $\gamma = \epsilon$). We investigate this symmetry by expanding the roots of (3.6) as $\omega = \omega_0 + \epsilon\,\omega_{1,\mathrm{rad}} + \epsilon^2\,\omega_{2,\mathrm{rad}} + \cdots$ for cooling and $\omega = \omega_0 + \epsilon\,\omega_{1,\mathrm{fric}} + \epsilon^2\,\omega_{2,\mathrm{fric}} + \cdots$ for friction. In both cases we obtain the real frequency ω_0 given by (3.4) at leading order. The $O(\epsilon)$ corrections are both purely dissipative:

$$\omega_{1,\mathrm{rad}} = \tfrac{1}{2}\mathrm{i}\omega_0(-4\omega_0^2 + 2n + 1)/(k + 4\omega_0^3), \tag{3.7a}$$

$$\omega_{1,\mathrm{fric}} = \tfrac{1}{2}\mathrm{i}\omega_0(-4\omega_0^2 - 2n - 1 - 2k/\omega_0)/(k + 4\omega_0^3). \tag{3.7b}$$

Observing that $\omega_{1,\mathrm{rad}} + \mathrm{i}/2 = -(\omega_{1,\mathrm{fric}} + \mathrm{i}/2)$ establishes the symmetry about $\mathrm{Im}(\omega) = -\epsilon/2$ for the dispersion relation truncated at $O(\epsilon)$.

3.2. *Thermal shallow water equations*

We now follow the same procedure for the thermal shallow water equations (1.2). We again consider an equatorial beta-plane, and we linearise for small perturbations about a state of rest with uniform depth h_0 and uniform buoyancy Θ_0,

$$h'_t + u'_x + v'_y = 0, \tag{3.8a}$$

$$\Theta'_t = -\kappa\,(h' + \Theta'), \tag{3.8b}$$

$$u'_t - \tfrac{1}{2}yv' + h'_x + \tfrac{1}{2}\Theta'_x = -\gamma u', \tag{3.8c}$$

$$v'_t + \tfrac{1}{2}yu' + h'_y + \tfrac{1}{2}\Theta'_y = -\gamma v'. \tag{3.8d}$$

We have non-dimensionalised as before, but we introduce Θ_0 as the buoyancy scale, and take $c = \sqrt{h_0\Theta_0}$ as the velocity scale. The four equations (3.8) may again be combined into the single ODE (3.2) for $\hat{v}(y)$, with coefficients

$$A = \frac{1}{4}\frac{\omega\,(\omega + \mathrm{i}\kappa)}{(\omega + \mathrm{i}\gamma)\,(\omega + \mathrm{i}\kappa/2)}, \quad B = \frac{\omega\,(\omega + \mathrm{i}\gamma)\,(\omega + \mathrm{i}\kappa)}{\omega + \mathrm{i}\kappa/2} - k^2 - \frac{k}{2\,(\omega + \mathrm{i}\gamma)}, \tag{3.9}$$

so the dispersion relation for equatorially trapped waves is

$$\frac{\omega\,(\omega + \mathrm{i}\gamma)\,(\omega + \mathrm{i}\kappa)}{\omega + \mathrm{i}\kappa/2} - k^2 - \frac{k}{2\,(\omega + \mathrm{i}\gamma)} = \left(n + \frac{1}{2}\right)\left(\frac{\omega\,(\omega + \mathrm{i}\kappa)}{(\omega + \mathrm{i}\gamma)\,(\omega + \mathrm{i}\kappa/2)}\right)^{1/2}. \tag{3.10}$$

Figure 10 shows the real and imaginary parts of the complex frequency ω for the first few equatorial Rossby waves ($n = 1, 2, 3$) and three different sets of κ and γ values. Again, the real part of ω is virtually unchanged by weak dissipation ($\kappa = 0.002$ or $\gamma = 0.001$), while $\mathrm{Im}(\omega)$ becomes negative. Figure 10 closely resembles our earlier figure 9, but we have doubled κ to 0.002. A perturbation analysis similar to before shows that $\mathrm{Im}(\omega)$ is symmetric about $-\epsilon/2$ between the cases of small cooling ($\kappa = 2\epsilon$ and $\gamma = 0$) and small friction ($\kappa = 0$ and $\gamma = \epsilon$).

4. Acceleration of the zonal mean zonal flow

We now calculate the acceleration of the zonal mean zonal flow caused by these solutions for decaying equatorially trapped Rossby waves.

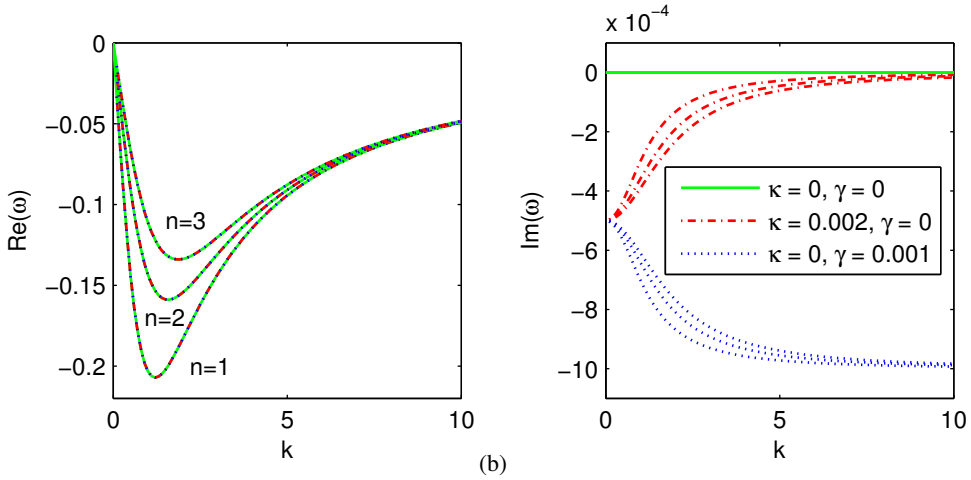

FIGURE 10. The real and imaginary parts of the dimensionless equatorial Rossby wave frequency ω for the thermal shallow water model with no dissipation, dissipation by cooling alone, and dissipation by friction alone.

4.1. *Height-damped shallow water equations*

We consider the full version of the unforced height-damped shallow water model (1.1) on an equatorial beta-plane. Combining the mass equation with the zonal momentum equation, gives the flux form of the zonal momentum equation,

$$(hu)_t + \left(hu^2 + \tfrac{1}{2}h^2\right)_x + (huv)_y - \tfrac{1}{2}yhv = -\gamma hu - \kappa u\,(h-1)\,, \tag{4.1}$$

using the non-dimensionalisation of §3.1. Following standard practice (Andrews & McIntyre 1976; Eliassen & Palm 1961; Vallis 2006) we decompose the velocity and other fields as $\boldsymbol{u} = \langle \boldsymbol{u}\rangle + \boldsymbol{u}'$ into a zonal average $\langle \boldsymbol{u}\rangle$ and a deviation $\boldsymbol{u}'$. Combining the zonal average of (4.1) with the zonal average of the dimensionless mass conservation equation,

$$\langle h\rangle_t + \langle hv\rangle_y = -\kappa\,(\langle h\rangle - 1)\,, \tag{4.2}$$

gives the zonal mean zonal momentum equation

$$\langle u\rangle_t = \underbrace{\langle v\rangle^*\left(\tfrac{1}{2}y - \langle u\rangle_y\right)}_{\text{Term 1}} \underbrace{- \frac{1}{\langle h\rangle}\partial_y\langle (hv)'\,u'\rangle}_{\text{Term 2}} \underbrace{- \frac{\kappa}{\langle h\rangle}\langle h'u'\rangle}_{\text{Term 3}} \underbrace{- \gamma\langle u\rangle^*}_{\text{Term 4}} \underbrace{- \frac{1}{\langle h\rangle}\langle h'u'\rangle_t}_{\text{Term 5}}\,. \tag{4.3}$$

We define $\langle a\rangle^* = \langle ha\rangle/\langle h\rangle$ to be the mass-weighted zonal mean of a quantity a (Showman & Polvani 2011; Thuburn & Lagneau 1999). Term 1 is the zonal acceleration due to the advection of absolute vorticity by the mean meridional circulation. Term 2 is the zonal acceleration due to the convergence of the shallow water Eliassen–Palm flux $\langle (hv)'u'\rangle$ (Thuburn & Lagneau 1999). Terms 3 and 4 are the zonal accelerations due directly to cooling and friction, respectively. Term 5 is the zonal acceleration due to the rate of change of zonal eddy momentum.

We now evaluate these general expressions for the equatorially trapped Rossby wave solutions from section §3.1. These represent small perturbations about a state of rest with unit depth in dimensionless variables. The meridional velocity perturbation is $v' = \mathrm{Re}\{\hat{v}(y)\exp(\mathrm{i}(kx-\omega t))\}$, with $\hat{v}(y)$ defined by (3.3) and (3.5). The corresponding zonal velocity and height perturbations are $u' = \mathrm{Re}\{\hat{u}(y)\exp(\mathrm{i}(kx-\omega t))\}$ and $h' = \mathrm{Re}\{\hat{h}(y)\exp(\mathrm{i}(kx-\omega t))\}$, where

$$\hat{u}(y) = \mathrm{i}\left(\frac{k\,(\mathrm{d}\hat{v}/\mathrm{d}y) - \frac{1}{2}y\,(\omega+\mathrm{i}\kappa)\,\hat{v}}{k^2 - (\omega+\mathrm{i}\gamma)\,(\omega+\mathrm{i}\kappa)}\right), \quad \hat{h}(y) = -\mathrm{i}\left(\frac{(\mathrm{i}\omega-\gamma)\,\hat{u} + \frac{1}{2}y\hat{v}}{k}\right), \tag{4.4}$$

for $k \neq 0$. The vanishing denominator at $k^2 = (\omega+\mathrm{i}\gamma)\,(\omega+\mathrm{i}\kappa)$ in $\hat{u}(y)$ gives the dispersion relation for Kelvin waves, which are distinguished by having zero meridional velocity ($\hat{v} = 0$).

Using standard formulae for the averages of products, the five terms on the right-hand side of (4.3) are

$$\langle v\rangle^* \left(\tfrac{1}{2}y - \langle u\rangle_y\right) = \tfrac{1}{4}y\,\mathrm{Re}\{\hat{h}(y)\hat{v}(y)^\star\}, \tag{4.5a}$$

$$-\frac{1}{\langle h\rangle}\partial_y\langle (hv)'\,u'\rangle = -\partial_y\langle u'v'\rangle = -\partial_y\left(\tfrac{1}{2}\,\mathrm{Re}\{\hat{u}(y)\hat{v}(y)^\star\}\right), \tag{4.5b}$$

$$-\frac{\kappa}{\langle h\rangle}\langle h'u'\rangle = -\tfrac{1}{2}\kappa\,\mathrm{Re}\{\hat{h}(y)\hat{u}(y)^\star\}, \tag{4.5c}$$

$$-\gamma\langle u\rangle^* = -\tfrac{1}{2}\gamma\,\mathrm{Re}\{\hat{h}(y)\hat{u}(y)^\star\}, \tag{4.5d}$$

$$-\frac{1}{\langle h\rangle}\langle h'u'\rangle_t = -\tfrac{1}{2}\,\mathrm{Re}\{-\mathrm{i}\omega\hat{h}(y)\hat{u}(y)^\star\} - \tfrac{1}{2}\,\mathrm{Re}\{\hat{h}(y)\,(-\mathrm{i}\omega\hat{u}(y))^\star\}, \tag{4.5e}$$

where a superscript * denotes a complex conjugate. All five terms are quadratic in the perturbation quantities, and thus proportional to the square of the wave amplitude. Our normalisation is given by the expression (3.3) for $\hat{v}$. We have omitted a cubic contribution $-\partial_y\langle h'u'v'\rangle$ from (4.5*b*) since perturbations are assumed to be small. The total zonal acceleration $\langle u\rangle_t$ is the sum of these five terms.

All five terms are identically zero for undamped ($\kappa = \gamma = 0$) equatorially trapped Rossby waves, since ω, A, and $\hat{v}$ are all real, while $\hat{u}$ and $\hat{h}$ are purely imaginary. Figure 11 shows $\langle u\rangle_t$ as a function of y for equatorial Rossby waves with $n = 1, 2, 3$ as damped by friction alone ($\kappa = 0$ and $\gamma = 0.001$) and by cooling alone ($\kappa = 0.001$ and $\gamma = 0$). The y-dependence of $\langle u\rangle_t$ for waves with $n = 1, 2, 3$ dissipated by cooling ($\kappa > 0$) implies $\langle u\rangle_t > 0$ in a region near the equator. This is consistent with the formation of a super-rotating equatorial jet. For $n = 1$ the tips of the two near-equatorial peaks are located at $\pm 7°$, while for $n = 3$ the tips of the two near-equatorial peaks are located at $\pm 6°$. For $n = 2$ the large eastward peak extends from roughly $-7°$ to $7°$ latitude. The latitudinal structure of $\langle u\rangle_t$ is thus consistent with the locations of the two "horns", local maxima of the eastward velocity, near the edges of the broad Jovian equatorial jet shown in figure 1.

Conversely, the $\langle u\rangle_t$ for frictionally dissipated waves shown in figure 11 is negative near the equator, consistent with the formation of a sub-rotating equatorial jet. A perturbation analysis similar to that in §3.1 shows that $\langle u\rangle_t$ due to weak cooling ($\kappa = \epsilon$ and $\gamma = 0$) is equal to minus the $\langle u\rangle_t$ due to weak friction ($\gamma = \epsilon$ and $\kappa = 0$). As figure 11 suggests, there is a line of symmetry about zero between the cases of small cooling and small friction. Moreover, $\langle u\rangle_t$ is very small at the equator for both friction and cooling when n is odd. Increasing k while keeping n, κ and γ fixed decreases the magnitude of $\langle u\rangle_t$ without changing its general shape. Increasing one of κ or γ while keeping k and n fixed increases the magnitude of $\langle u\rangle_t$ without changing its general shape.

Figure 12 shows the five separate terms in (4.3) alongside their sum $\langle u\rangle_t$ for $n = k = 1$ and dissipation due to either friction or cooling. In both cases, the sum is close to the contribution from Term 2, the Eliassen–Palm flux convergence, alone. The other terms are all smaller. The contribution from the advection of absolute vorticity by the mean meridional circulation is directed westward for dissipation due to friction, and eastward for dissipation due to cooling. The same conclusion holds for $n = 2$, shown in figure 13, except Terms 3,4,5 vanish at the equator. The five terms for $n = 3$ (not plotted) closely resemble those shown for $n = 1$.

4.2. *Thermal shallow water equations*

We now compute the zonal acceleration due to Rossby waves for the unforced thermal shallow water model (1.2). The corresponding zonal mean zonal momentum equation is

$$\langle u\rangle_t = \underbrace{\langle v\rangle^* \left(\tfrac{1}{2}y - \langle u\rangle_y\right)}_{\text{Term 1}} \underbrace{- \frac{1}{\langle h\rangle}\partial_y\langle (hv)'\,u'\rangle}_{\text{Term 2}} \underbrace{- \gamma\langle u\rangle^*}_{\text{Term 4}} \underbrace{- \frac{1}{\langle h\rangle}\langle h'u'\rangle_t}_{\text{Term 5}}. \tag{4.6}$$

There is no explicit cooling term proportional to κ, because cooling appears only in the temperature equation. However, we label the four terms as Term 1, Term 2, Term 4, and Term 5 to aid comparison with §4.1. The meridional velocity perturbation for an equatorial Rossby wave is again $v' = \mathrm{Re}\{\hat{v}(y)\exp(\mathrm{i}(kx - \omega t))\}$, with $\hat{v}(y)$ defined by (3.3) and (3.9). The corresponding perturbations to the height, buoyancy, and zonal velocity take the same functional forms, with

$$\hat{h}(y) = -\mathrm{i}\left(\frac{\mathrm{i}k\hat{u} + \mathrm{d}\hat{v}/\mathrm{d}y}{\omega}\right), \qquad \hat{\Theta}(y) = -\mathrm{i}\left(\frac{\kappa\hat{h}}{\omega + \mathrm{i}\kappa}\right),$$
$$\hat{u}(y) = \mathrm{i}\left(\frac{k\,(1 + \mathrm{i}\kappa/\,(2\omega))\,\mathrm{d}\hat{v}/\mathrm{d}y - \frac{1}{2}y\,(\omega + \mathrm{i}\kappa)\,\hat{v}}{k^2\,(1 + \mathrm{i}\kappa/\,(2\omega)) - (\omega + \mathrm{i}\gamma)\,(\omega + \mathrm{i}\kappa)}\right), \tag{4.7}$$

for $\omega \neq 0$ and $\omega \neq -\mathrm{i}\kappa$. The remaining vanishing denominator for $\hat{u}$ at $k^2 = (\omega + \mathrm{i}\gamma)\,(\omega + \mathrm{i}\kappa)\,/\,(1 + \mathrm{i}\kappa/\,(2\omega))$ gives the dispersion relation for the equatorial Kelvin waves as modified by friction and cooling.

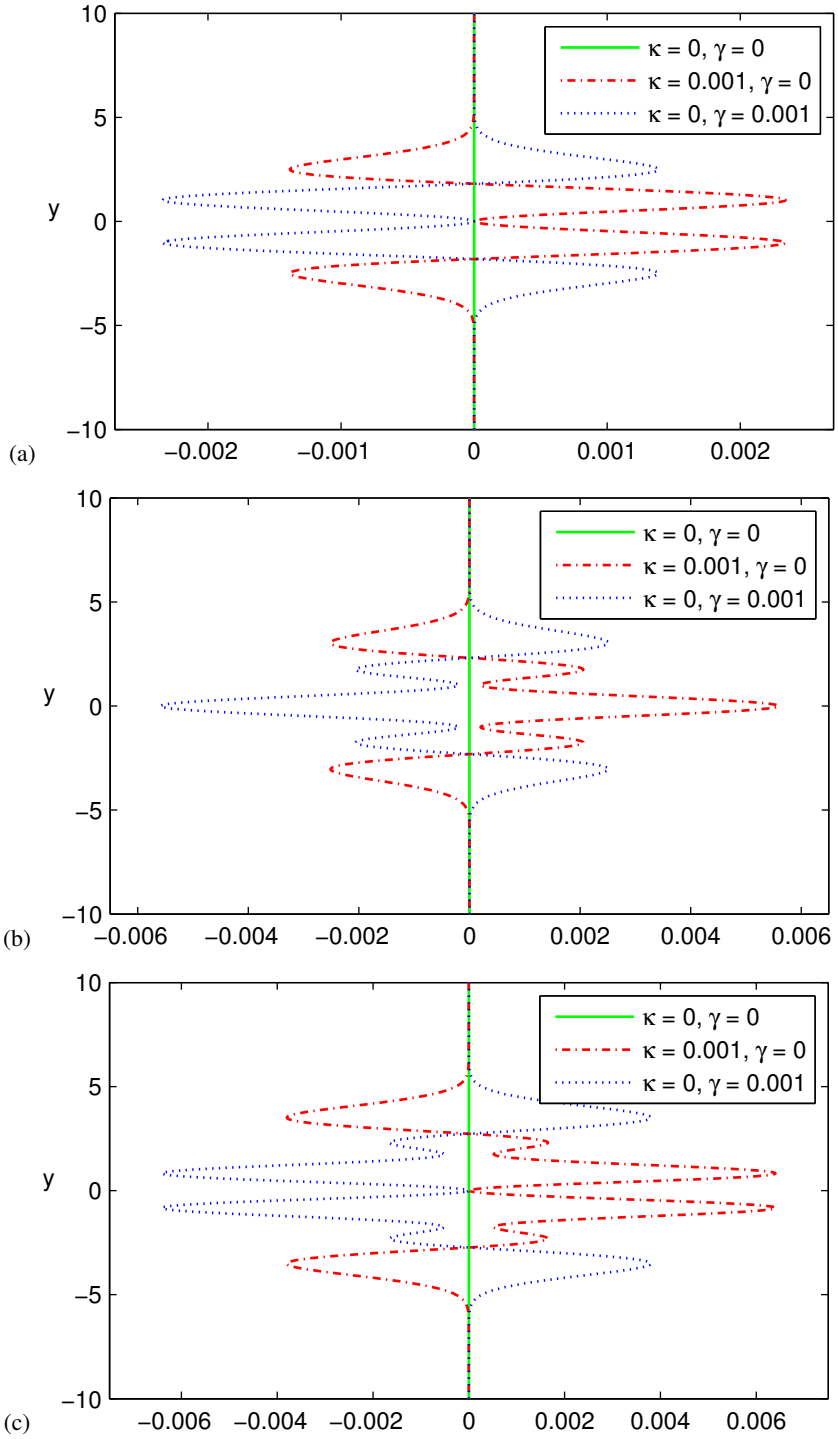

FIGURE 11. The sum of the five zonal acceleration terms on the right-hand side of (4.3) for the three cases of no dissipation, dissipation by cooling ($\kappa \neq 0$) and dissipation by friction ($\gamma \neq 0$). All terms are plotted for $k = 1$. Plots (a), (b), (c) correspond to $n = 1, 2, 3$ respectively.

Figure 14 shows the net zonal acceleration $\langle u \rangle_t$ generated by dissipation by friction alone, and by cooling alone, for the first three equatorial Rossby waves $n = 1, 2, 3$ with $k = 1$. Again, all terms are identically zero in the absence of dissipation. For $n = 2$ and dissipation by cooling, $\langle u \rangle_t > 0$ in a region near the equator. For $n = 1$ and $n = 3$, $\langle u \rangle_t < 0$ in a very small region close to the equator. However, $\langle u \rangle_t > 0$ from -7° to -2° and from 2° to 7° for $n = 1$. For $n = 3$, $\langle u \rangle_t > 0$ from -12° to -1° and from 1° to 12°. Moreover, the positive $\langle u \rangle_t$ at the equator for $n = 2$ is far larger in magnitude than the negative accelerations created at the equator by decaying waves with comparable amplitude and $n = 1$ or $n = 3$. The tips of the two equatorial peaks are located at $\pm 5^\circ$ for $n = 1$ and $n = 3$, while for $n = 2$ the

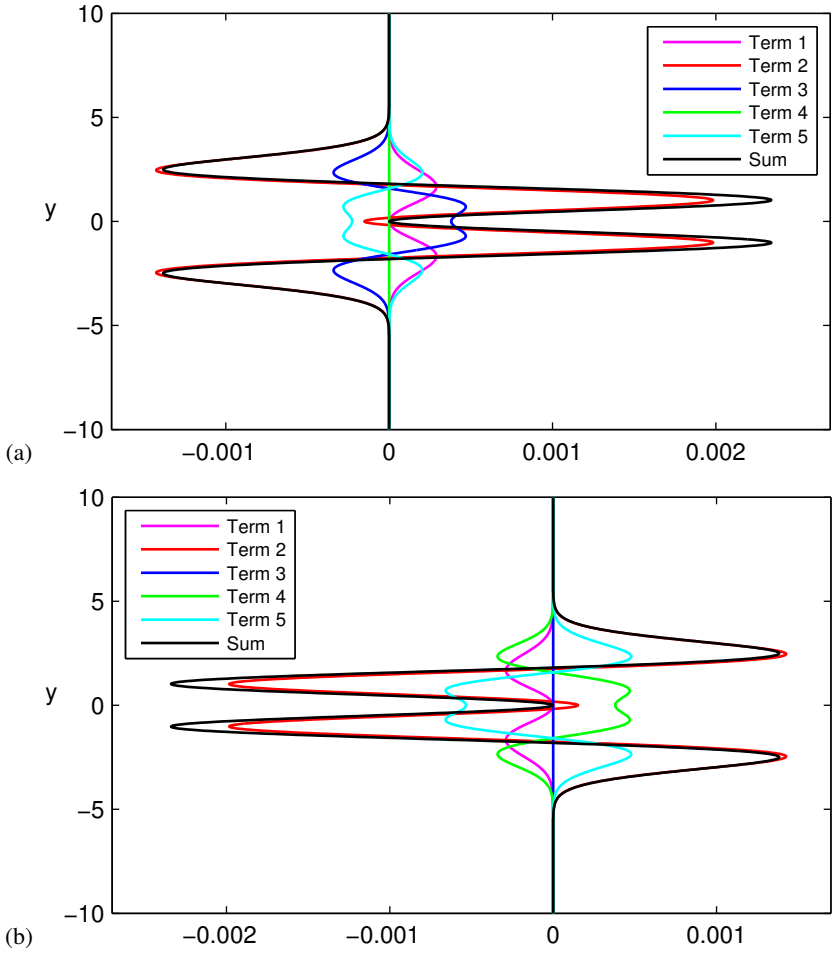

FIGURE 12. The five zonal acceleration terms from the right-hand side of (4.3), and their sum, for (a) dissipation solely by cooling ($\kappa = 0.001, \gamma = 0$) and (b) dissipation solely by friction ($\kappa = 0, \gamma = 0.001$). All terms are calculated for $n = k = 1$.

large eastward peak extends from roughly -7° to 7°. The latitudinal structure of $\langle u \rangle_t$ is thus again consistent with the formation of a super-rotating equatorial jet through dissipation by cooling, and with the locations of the two peaks of maximal eastward velocity in the broad Jovian equatorial jet at $\pm 7^\circ$ shown in figure 1.

The corresponding data for frictionally dissipated waves in figure 14 show that $\langle u \rangle_t < 0$ in regions near the equator for $n = 1, 2, 3$, again consistent with the formation of sub-rotating equatorial jets. There is now no line of symmetry between the accelerations due to small cooling and small friction. However, increasing k while keeping n, κ and γ fixed decreases the magnitude of $\langle u \rangle_t$ in both cases. Increasing κ or γ for fixed k and n increases the magnitude of $\langle u \rangle_t$.

Figures 15 and 16 show the four separate terms from (4.6) for the cases of dissipation solely by either cooling or friction for waves with $k = 1$, and $n = 1$ and $n = 2$ respectively. Term 2, the Eliassen–Palm flux convergence, is primarily responsible for the positive zonal acceleration in the near-equatorial region due to cooling for $n = 1$. However, the net zonal acceleration at higher latitudes created by cooling is now primarily due to Term 1, the advection of absolute vorticity by the mean meridional circulation. This term creates large, negative values of $\langle u \rangle_t$ at higher latitudes. By contrast, the Eliassen–Palm flux convergence was the dominant contribution at all latitudes in the height-damped shallow water model.

For dissipation by friction and $n = 1$, the Eliassen–Palm flux convergence contributes a positive zonal acceleration close to the equator, but is outweighed by a large, negative contribution from Term 5 due to changes in $\langle h'u' \rangle$. At other latitudes, the Eliassen–Palm flux convergence is the dominant contribution. For $n = 2$, the Eliassen–Palm flux convergence is the dominant contribution to $\langle u \rangle_t$ at all latitudes, except for two intermediate regions where Term 5 is both dominant and negative. For $n = 3$ (not shown) the Eliassen–Palm flux convergence is again the main contribution to $\langle u \rangle_t$ near the equator.

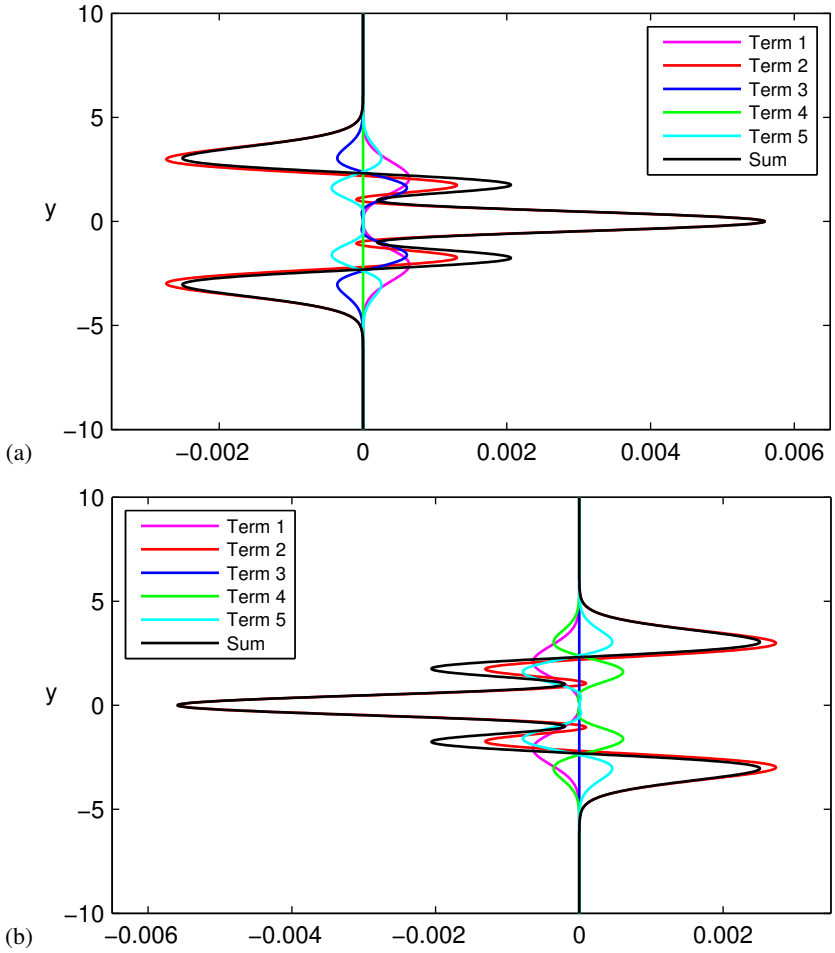

FIGURE 13. The five zonal acceleration terms from the right-hand side of (4.3), and their sum, for (a) dissipation solely by cooling ($\kappa = 0.001, \gamma = 0$) and (b) dissipation solely by friction ($\kappa = 0, \gamma = 0.001$). All terms are calculated for $n = 2$ and $k = 1$.

4.3. *Discussion*

We have performed a similar analysis for decaying equatorially trapped Kelvin, Yanai, and inertia-gravity waves in our height-damped and thermal models. The zonal accelerations due to these waves are at least an order of magnitude smaller than those due to decaying Rossby waves of the same amplitude. Thus, as expected from our global quasi-geostrophic simulations, these other types of wave make no significant contribution to setting the direction of the equatorial jet.

Our simulation parameters gave a dimensionless cooling rate $\kappa = 0.00788$ roughly 23 times larger than our dimensionless frictional rate $\gamma = 0.000342$. In §4.1 we established an antisymmetry in $\langle u \rangle_t$ between the cases of small cooling ($\kappa = \epsilon$ and $\gamma = 0$) and small friction ($\kappa = 0$ and $\gamma = \epsilon$) for the height-damped shallow water equations. For $\kappa \gg \gamma$, our theory gives $\langle u \rangle_t > 0$ in a region near the equator, consistent with the super-rotating equatorial jet in our simulation. Conversely, for the purely frictional case ($\kappa = 0$) the zonal mean zonal acceleration is negative throughout the equatorial region (see figure 11), consistent with the sub-rotating equatorial jet in our simulation.

No corresponding symmetry between κ and γ exists in our thermal shallow water model, but the analogue of figure 14 for $\kappa = 0.00788$ and $\gamma = 0.000342$ shows that the positive magnitude of $\langle u \rangle_t$ due to dissipation by cooling is significantly larger than the negative magnitude of $\langle u \rangle_t$ due to dissipation by friction in the equatorial region. Our theory thus suggests $\langle u \rangle_t > 0$ in the equatorial region, again consistent with the formation of a super-rotating equatorial jet in our simulations. For $n = 1$ and $n = 3$ there is a very small region at the equator where decaying Rossby waves produce $\langle u \rangle_t < 0$, but there is a much larger positive contribution from $n = 2$. Our theory thus still suggests a super-rotating equatorial jet, if we assume that waves with even and odd n are excited with comparable amplitudes.

5. Conclusions

Numerical simulations of shallow water equations on a sphere with isotropic random forcing reliably produce mixtures of coherent vortices and alternating zonal jets. These simulations typically include Rayleigh friction to absorb the

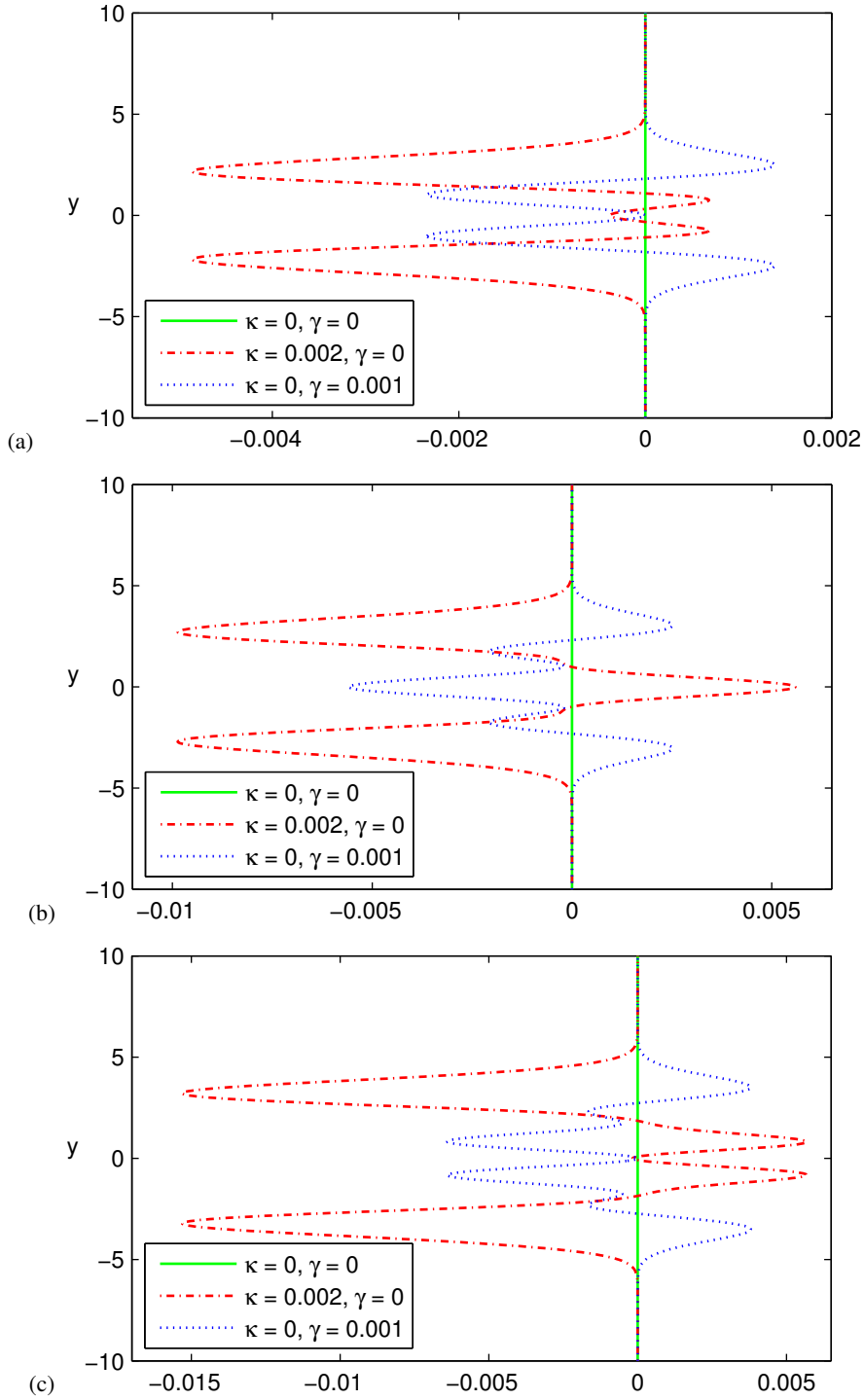

FIGURE 14. The sum of the four zonal acceleration terms on the right-hand side of (4.6) for the three cases of no dissipation, dissipation by cooling alone, and dissipation by friction alone. All terms are plotted for $k = 1$. Plots (a),(b),(c) correspond to $n = 1, 2, 3$ respectively.

gradual inverse cascade of energy past the Rhines scale that otherwise causes the zonal jets to break up into domain-sized coherent vortices after very long times. Such simulations invariably produce sub-rotating equatorial jets when run with Jovian parameters (Vasavada & Showman 2005). However, simulations that model radiative effects by relaxing the height field produce a super-rotating equatorial jet (Scott & Polvani 2007, 2008), as do simulations of the thermal shallow water equations with a Newtonian cooling term in their separate temperature equation (see §2 and Warneford & Dellar 2014). Simulations of the global quasi-geostrophic versions of these three different models produce equatorial jets in the same directions as their parent models (Warneford 2014).

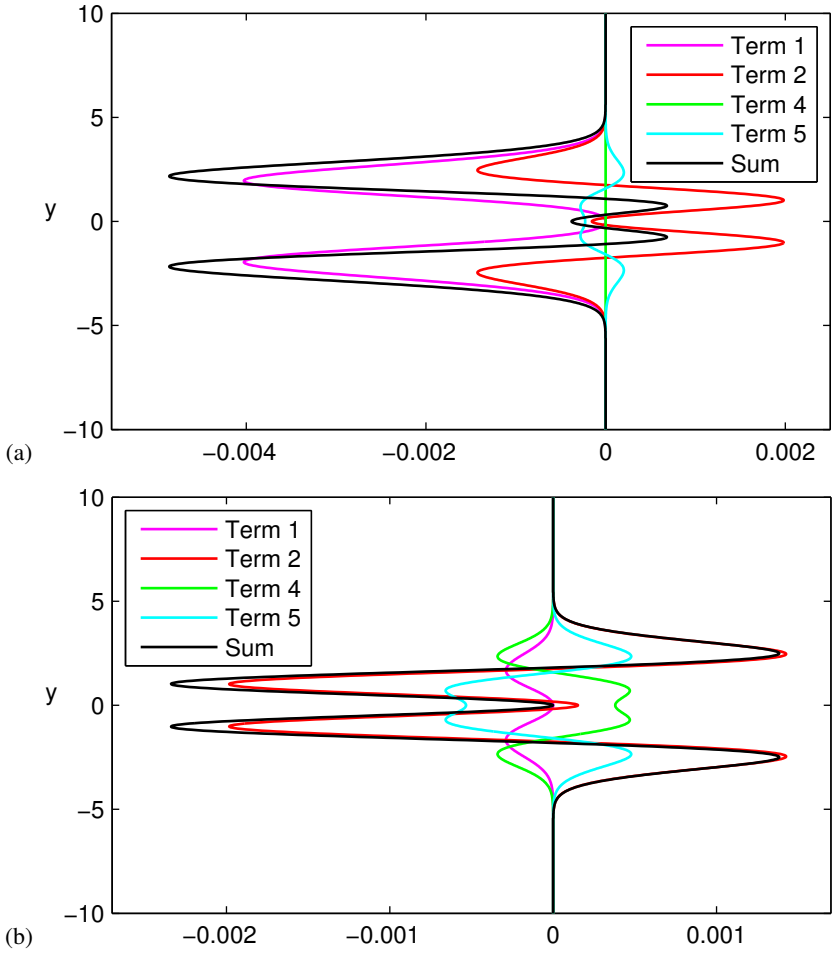

FIGURE 15. The zonal acceleration terms from the right-hand side of (4.6), and their sum, for (a) dissipation by cooling alone ($\kappa = 0.002, \gamma = 0$) and (b) dissipation by friction alone ($\kappa = 0, \gamma = 0.001$). All terms are plotted for $n = k = 1$.

We have provided an explanation for the different directions of the equatorial jets in the three different models. We identified the different contributions to the equation for $\langle u \rangle_t$, the zonal mean zonal acceleration, for small perturbations to a uniform rest state, and evaluated them for equatorially trapped Rossby waves decaying through a combination of Newtonian cooling and Rayleigh friction. For the standard shallow water equations, with or without height-damping, the resulting zonal acceleration arises predominantly from the convergence of the Eliassen–Palm flux $\langle u'v' \rangle$ due to small-amplitude disturbances in shallow water. This flux vanishes for undamped Rossby waves, due to the phase relation between u' and v'. Dissipation alters this phase relation to create a net flux of zonal momentum in the meridional direction. The varying spatial structure of this flux for different values of the dissipation parameters is consistent with the formation of super-rotating equatorial jets in simulations damped primarily by Newtonian cooling, and the formation of sub-rotating equatorial jets in simulations damped solely by Rayleigh friction. Moreover, the spatial structure is consistent with the presence and locations of two "horns", or peaks of maximal eastward velocity, near the edges of the broad Jovian equatorial jet, and a slightly smaller velocity precisely on the equator (see figure 1).

We also performed an equivalent analysis for our thermal shallow water model. The overall zonal mean zonal acceleration $\langle u \rangle_t$ due to equatorially trapped Rossby waves decaying due to Newtonian cooling is again consistent with the formation of super-rotating equatorial jets in simulations for which cooling is the primary source of dissipation. However, the Eliassen–Palm flux convergence is only the largest contribution to $\langle u \rangle_t$ very close to the equator. Instead, the zonal acceleration due to the advection of absolute vorticity by the mean meridional circulation dominates at higher latitudes. Moreover, a net positive $\langle u \rangle_t$ at the equator only arises from Newtonian cooling if the positive contributions from even mode numbers ($n = 2$ is shown) outweigh the smaller negative contributions from odd mode numbers ($n = 1$ and $n = 3$ are shown) under the assumption that both odd and even wave modes are excited with roughly equal amplitudes.

Our work relies upon two major simplifying assumptions. We considered trapped equatorial Rossby waves on a background rest state, which allowed us to use the known analytical expressions for these waves in terms of Hermite polynomials. A more complete theory would calculate the Rossby wave spectrum supported by a background mean

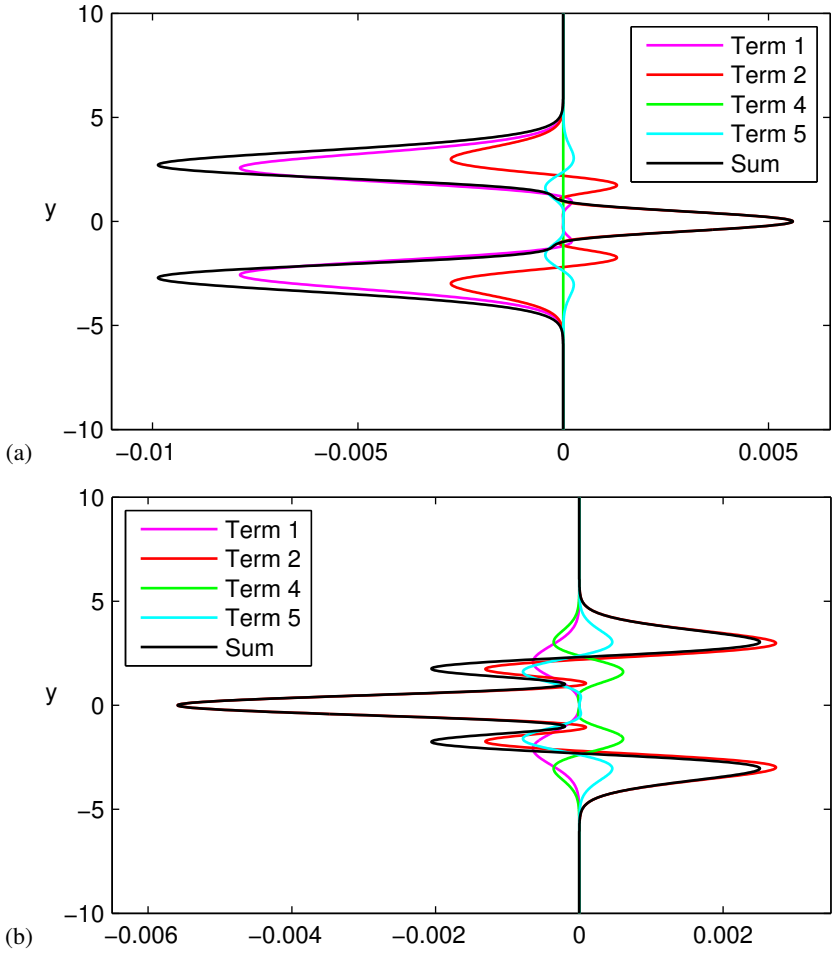

FIGURE 16. The zonal acceleration terms from the right-hand side of (4.6), and their sum, for (a) dissipation by cooling alone ($\kappa = 0.002, \gamma = 0$) and (b) dissipation by friction alone ($\kappa = 0, \gamma = 0.001$). All terms are plotted for $n = 2$ and $k = 1$.

zonal flow $\overline{u}(y)$. Secondly, we calculated the mean zonal accelerations due to freely decaying Rossby waves. We thus assumed that the waves are excited by sources outside the equatorial region, and neglected the effect of this excitation on the zonal mean flow. Some support for this second assumption is offered by the profiles shown in figures 6 and 7 for the quantity R' used by Sardeshmukh & Hoskins (1988) to diagnose sources of Rossby waves. These sources are located predominantly away from the equatorial regions in our simulations. Although our work falls short of a full wave-mean flow interaction theory in these two respects, we believe it offers at least a step towards a theoretical explanation of the origins of equatorial super- or sub-rotation in numerical simulations.

We thank Michael McIntyre for a very detailed and stimulating referee report on an earlier manuscript, and Ted Johnson for useful conversations. This work was supported by the Engineering and Physical Sciences Research Council through a Doctoral Training Grant award to E.S.W. and an Advanced Research Fellowship [grant number EP/E054625/1] to P.J.D. The computations employed the University of Oxford's Advanced Research Computing facilities, and the Emerald GPU cluster of the e-Infrastructure South Centre for Innovation.

REFERENCES

ANDREWS, D.G. & MCINTYRE, M.E. 1976 Planetary waves in horizontal and vertical shear: The generalized Eliassen–Palm relation and the mean zonal acceleration. *J. Atmos. Sci.* **33**, 2031–2048.

ARNOLD, N. P., TZIPERMAN, E. & FARRELL, B. 2012 Abrupt transition to strong superrotation driven by equatorial wave resonance in an idealized GCM. *J. Atmos. Sci.* **69**, 626–640.

ATKINSON, D. H., POLLACK, J. B. & SEIFF, ALVIN 1998 The Galileo Probe Doppler wind experiment: Measurement of the deep zonal winds on Jupiter. *J. Geophys. Res.* **103**, 22911–22928.

BEEBE, R. 1994 Characteristic zonal winds and long-lived vortices in the atmospheres of the outer planets. *Chaos* **4**, 113–122.

CHARNEY, J. G. & STERN, M. E. 1962 On the stability of internal baroclinic jets in a rotating atmosphere. *J. Met.* **19**, 159–172.

CHO, J. Y-K. & POLVANI, L. M. 1996*a* The emergence of jets and vortices in freely evolving, shallow-water turbulence on a sphere. *Phys. Fluids* **8**, 1531–1552.

CHO, J. Y-K. & POLVANI, L. M. 1996*b* The morphogenesis of bands and zonal winds in the atmospheres on the giant outer planets. *Science* **273**, 335–337.

DOWLING, T. E. 1995 Estimate of Jupiter's deep zonal-wind profile from Shoemaker–Levy 9 data and Arnol'd's second stability criterion. *Icarus* **117**, 439–442.

DOWLING, T. E. & INGERSOLL, A. P. 1989 Jupiter's Great Red Spot as a shallow water system. *J. Atmos. Sci.* **46**, 3256–3278.

ELIASSEN, A. & PALM, E. 1961 On the transfer of energy in stationary mountain waves. *Geofys. Publ.* **22**, 1–23.

GILL, A. E. 1982 *Atmosphere Ocean Dynamics*. New York: Academic Press.

HIDE, R. 1969 Dynamics of the atmospheres of the major planets with an appendix on the viscous boundary layer at the rigid bounding surface of an electrically-conducting rotating fluid in the presence of a magnetic field. *J. Atmos. Sci.* **26**, 841–853.

HOU, T. Y. & LI, R. 2007 Computing nearly singular solutions using pseudo-spectral methods. *J. Comp. Phys.* **226**, 379–397.

HUPCA, IOAN OVIDIU, FALCOU, JOEL, GRIGORI, LAURA & STOMPOR, RADEK 2012 Spherical harmonic transform with GPUs. *Lecture Notes in Computer Science* **7155**, 355–366.

IACONO, R., STRUGLIA, M. V. & RONCHI, C. 1999*a* Spontaneous formation of equatorial jets in freely decaying shallow water turbulence. *Phys. Fluids* **11**, 1272–1274.

IACONO, R., STRUGLIA, M. V., RONCHI, C. & NICASTRO, S. 1999*b* High-resolution simulations of freely decaying shallow-water turbulence on a rotating sphere. *Il Nuovo Cimento C* **22**, 813–821.

IMAMURA, TAKESHI, HORINOUCHI, TAKESHI & DUNKERTON, T. J. 2004 The lateral transport of zonal momentum due to Kelvin waves in a meridional circulation. *J. Atmos. Sci.* **61**, 1966–1975.

INGERSOLL, A. P. 1990 Atmospheric dynamics of the outer planets. *Science* **248**, 308–315.

INGERSOLL, A. P., DOWLING, T. E., GIERASCH, P. J., ORTON, G. S., READ, P. L., SÁNCHEZ-LAVEGA, A., SHOWMAN, A. P., SIMON-MILLER, A. A. & VASAVADA, A. R. 2007 Dynamics of Jupiter's atmosphere. In *Jupiter: The Planet, Satellites and Magnetosphere* (ed. F. Bagenal, T. E. Dowling & W. B. McKinnon), pp. 105–128. Cambridge: Cambridge University Press.

JUCKES, MARTIN 1989 A shallow water model of the winter stratosphere. *J. Atmos. Sci.* **46**, 2934–2956.

KHOUIDER, BOUALEM, MAJDA, ANDREW J. & STECHMANN, SAMUEL N. 2013 Climate science in the tropics: waves, vortices and PDEs. *Nonlinearity* **26**, R1–R68.

KUO, H. L. 1959 Finite-amplitude three-dimensional harmonic waves on the spherical earth. *J. Meteorol.* **16**, 524–534.

LAVOIE, R. L. 1972 A mesoscale numerical model of lake-effect storms. *J. Atmos. Sci.* **29**, 1025–1040.

LILLY, D. K. 1969 Numerical simulation of two-dimensional turbulence. *Phys. Fluids* **12**, II–240–II–249.

LIMAYE, S. S. 1986 Jupiter: New estimates of the mean zonal flow at the cloud level. *Icarus* **65**, 335–352.

MAJDA, A. J. & KLEIN, RUPERT 2003 Systematic multiscale models for the tropics. *J. Atmos. Sci.* **60**, 393–408.

MARCUS, P. S. 1988 Numerical simulation of Jupiter's Great Red Spot. *Nature* **331**, 693–696.

MATSUNO, T. 1966 Quasi-geostrophic motions in the equatorial area. *J. Meteorol. Soc. Japan* **44**, 25–43.

MCCREARY, J. P. 1985 Modeling equatorial ocean circulation. *Annu. Rev. Fluid Mech.* **17**, 359–409.

MCCREARY, J. P., FUKAMACHI, Y. & KUNDU, P. K. 1991 A numerical investigation of jets and eddies near an eastern ocean boundary. *J. Geophys. Res.* **96**, 2515–2534.

MCCREARY, J. P. & KUNDU, P. K. 1988 A numerical investigation of the Somali Current during the Southwest Monsoon. *J. Marine Res.* **46**, 25–58.

MCCREARY, J. P. & YU, Z. 1992 Equatorial dynamics in a $2\frac{1}{2}$-layer model. *Prog. Oceanogr.* **29**, 61–132.

POLVANI, L. M., WAUGH, D. W. & PLUMB, R. ALAN 1995 On the subtropical edge of the stratospheric surf zone. *J. Atmos. Sci.* **52**, 1288–1309.

PORCO, C. C., WEST, R. A., MCEWEN, A., DEL GENIO, A. D., INGERSOLL, A. P., THOMAS, P., SQUYRES, S., DONES, L., MURRAY, C. D., JOHNSON, T. V., BURNS, J. A., BRAHIC, A., NEUKUM, G., VEVERKA, J., BARBARA, J. M., DENK, T., EVANS, M., FERRIER, J. J., GEISSLER, P., HELFENSTEIN, P., ROATSCH, T., THROOP, H., TISCARENO, M. & VASAVADA, A. R. 2003 Cassini imaging of Jupiter's atmosphere, satellites, and rings. *Science* **299**, 1541–1547.

RHINES, P. B. 1975 Waves and turbulence on a beta-plane. *J. Fluid Mech.* **69**, 417–443.

RIPA, P. 1993 Conservation laws for primitive equations models with inhomogeneous layers. *Geophys. Astrophys. Fluid Dynam.* **70**, 85–111.

RIPA, P. 1995 On improving a one-layer ocean model with thermodynamics. *J. Fluid Mech.* **303**, 169–201.

RIPA, P. 1996*a* Linear waves in a one-layer ocean model with thermodynamics. *J. Geophys. Res.* **101**, 1233–1245.

RIPA, P. 1996*b* Low frequency approximation of a vertically averaged ocean model with thermodynamics. *Rev. Mex. Fís.* **41**, 117–135.

RØED, L. P. & SHI, X. B. 1999 A numerical study of the dynamics and energetics of cool filaments, jets, and eddies off the Iberian Peninsula. *J. Geophys. Res.* **104**, 29817–29841.

SARDESHMUKH, P. D. & HOSKINS, B. J. 1988 The generation of global rotational flow by steady idealized tropical divergence. *J. Atmos. Sci.* **45**, 1228–1251.

SCHNEIDER, TAPIO & LIU, JUNJUN 2009 Formation of jets and equatorial superrotation on jupiter. *J. Atmos. Sci.* **66**, 579–601.

SCHOPF, P. S. & CANE, M. A. 1983 On equatorial dynamics, mixed layer physics and sea surface temperature. *J. Phys. 0ceanogr.* **13**, 917–935.

SCHUBERT, W. H., TAFT, R. K. & SILVERS, L. G. 2009 Shallow water quasi-geostrophic theory on the sphere. *J. Adv. Model. Earth Syst.* **1**, 2.

SCOTT, R. K. & POLVANI, L. M. 2007 Forced-dissipative shallow-water turbulence on the sphere and the atmospheric circulation of the giant planets. *J. Atmos. Sci.* **64**, 3158–3176.

SCOTT, R. K. & POLVANI, L. M. 2008 Equatorial superrotation in shallow atmospheres. *Geophys. Res. Lett.* **35**, L24202.

SHOWMAN, A. P. 2007 Numerical simulations of forced shallow-water turbulence: Effects of moist convection on the large-scale circulation of Jupiter and Saturn. *J. Atmos. Sci.* **64**, 3132–3157.

SHOWMAN, A. P. & POLVANI, L. M. 2011 Equatorial superrotation on tidally locked exoplanets. *Astrophys. J.* **738**, 71.

SMITH, K. S. 2004 A local model for planetary atmospheres forced by small-scale convection. *J. Atmos. Sci.* **61**, 1420–1433.

SMITH, K. S., BOCCALETTI, G., HENNING, C. C., MARINOV, I., TAM, C. Y., HELD, I. M. & VALLIS, G. K. 2002 Turbulent diffusion in the geostrophic inverse cascade. *J. Fluid Mech.* **469**, 13–48.

SRINIVASAN, K. & YOUNG, W. R. 2012 Zonostrophic instability. *J. Atmos. Sci.* **69**, 1633–1656.

THUBURN, J. & LAGNEAU, V. 1999 Eulerian mean, contour integral, and finite-amplitude wave activity diagnostics applied to a single-layer model of the winter stratosphere. *J. Atmos. Sci.* **56**, 689–710.

VALLIS, G. K. 2006 *Atmospheric and Oceanic Fluid Dynamics*. Cambridge University Press.

VASAVADA, A. R. & SHOWMAN, A. P. 2005 Jovian atmospheric dynamics: an update after Galileo and Cassini. *Rep. Prog. Phys.* **68**, 1935–1996.

VERKLEY, W. T. M. 2009 A balanced approximation of the one-layer shallow-water equations on a sphere. *J. Atmos. Sci.* **66**, 1735–1748.

WALTERSCHEID, R. L., BRINKMAN, D. G. & SCHUBERT, G. 2000 Wave disturbances from the comet SL–9 impacts into Jupiter's atmosphere. *Icarus* **145**, 140–146.

WARNEFORD, E. S. 2014 *The thermal shallow water equations, their quasi-geostrophic limit, and applications to Jovian atmospheres*. DPhil thesis, University of Oxford, (in preparation).

WARNEFORD, E. S. & DELLAR, P. J. 2013 The quasi-geostrophic theory of the thermal shallow water equations. *J. Fluid Mech.* **723**, 374–403.

WARNEFORD, E. S. & DELLAR, P. J. 2014 Thermal shallow water models of geostrophic turbulence in Jovian atmospheres. *Phys. Fluids* **26**, 016603.

WILLIAMS, G. P. 1978 Planetary circulations: 1. Barotropic representation of Jovian and terrestrial turbulence. *J. Atmos. Sci.* **35**, 1399–1426.

WILLIAMS, G. P. & YAMAGATA, T. 1984 Geostrophic regimes, intermediate solitary vortices and Jovian eddies. *J. Atmos. Sci.* **41**, 453–478.